Bootstrap Embedding with an Unrestricted Mean-Field Bath

Henry K. Tran,[1] Hong-Zhou Ye,[1] and Troy Van Voorhis[1, a)]
Department of Chemistry, Massachusetts Institute of Technology, Cambridge, MA 02139, USA

(Dated: 5 November 2020)

A suite of quantum embedding methods have recently been developed where the Schmidt decomposition is applied to the full system wavefunction to derive basis states that preserve the entanglement between the fragment and bath. The quality of these methods can depend heavily on the quality of the initial full system wavefunction. Most of these methods, including bootstrap embedding (BE) [*J. Chem. Phys.*, **145**, 074102, (2016)], start from a spin-restricted mean-field wavefunction (call this RBE). Given that spin-unrestricted wavefunctions can capture a significant amount of strong correlation at the mean-field level, we suspect that starting from a spin-unrestricted mean-field wavefunction will improve these embedding methods for strongly correlated systems. In this work, BE is generalized to an unrestricted Hartree-Fock (UHF) bath (call this UBE) and UBE is applied to model hydrogen ring systems. UBE's improved versatility over RBE is utilized to calculate high spin symmetry states that were previously unattainable with RBE. Ionization potentials, electron affinities, and spin-splittings are computed using UBE with accuracy on par with spin-unrestricted coupled cluster singles and doubles (CCSD). Even for cases where RBE is viable, UBE converges more reliably. We discuss the limitations or weaknesses of each calculation and how improvements to RBE and DMET these past few years can also improve UBE.

I. INTRODUCTION

The development of correlated quantum chemical methods with sufficient accuracy and feasible efficiency remains an active area of research. Mean-field methods such as spin-restricted[1] and spin-unrestricted[2] Hartree-Fock (RHF and UHF) and density functional theory[3,4] (DFT) scale favorably with system size and thus, are popular for large systems.[5] The limitations of DFT for the exploration of materials are known,[6] motivating a need for more accurate, correlated methods. Popular first principle methods that capture electron correlation include configuration interaction (CI)[7] and coupled cluster (CC),[8] and the excited state variant of equation-of-motion CC (EOM-CC),[9] which has seen many applications in larger molecules[10] and solids.[11] However, these methods still scale steeply with system size, motivating the search for faster scaling methods.

An appealing compromise between the accuracy of these methods and low computational scaling are quantum embedding methods. In a quantum embedding method, the total degrees of freedom of the system are divided into a subset of important degrees, called the fragment, and a subset of the remaining degrees, called the bath. The fragment contains fewer degrees of freedom than the full system and can be treated with a high level of theory in less computer time. The bath, as well as the interaction between the fragment and bath, can be treated at a lower level of theory. A whole suite of different embedding methods have been designed with this philosophy in mind. One approach are projection based embedding methods[12] which include wavefunction theory (WFT)-in-DFT embedding[12–14] and DFT-in-DFT embedding.[15–17]

In this work, we focus on embedding methods derived from the Schmidt decomposition.[18] Seminal works on this type of embedding were on density matrix embedding theory (DMET) that proved to be effective for strongly correlated systems.[19,20] A variety of methods also based on the Schmidt decomposition have arisen since then including density embedding theory (DET),[21,22] projected site-occupation embedding theory (P-SOET),[23] and bootstrap embedding theory (BE).[24,25] The philosophy behind all of these theories is to derive bath states that preserve the entanglement between fragment and bath. These bath states are obtained from the Schmidt decomposition of the full system wavefunction for the electronic state of interest. Unless this wavefunction is the true wavefunction, the derived bath states capture less than the true entanglement between fragment and bath. Typically, the bath states are derived from a mean-field solution to the full system Hamiltonian and cannot provide a complete description of the entanglement. Each method has its own algorithm for improving upon the initial, approximate entanglement obtained from the system wavefunction.

These methods have seen a wide array of successful applications. DMET in its original papers found success on model systems and simple atomic lattices in 1D[19–21,26,27] and in 2D.[19,28–32] Since then, DMET has been applied to chemical systems to study chemical reactions,[32] bond dissociation,[33,34] non-equilibrium dynamics,[35], and simple solids with periodic boundary conditions.[22,34,36,37] While most of the literature has been focused on ground state electronic structure calculations, excited state variants have also been explored.[30,38–40] DMET methods fragment the system into a rigid set of non-overlapping fragments that leads to ambiguity in fragment choices

a)Electronic mail: tvan@mit.edu

and slow convergence with fragment size.[32] BE[24,25,41–44] addresses these issues by partitioning the system into a more flexible set of overlapping fragments, which can be chosen in a black-box manner,[43] and introduces a new set of inter-fragment matching conditions to improve convergence. BE has been applied to 1D and 2D model systems[24,25,41] and molecular systems.[42,43] Recently, we have implemented a more efficient BE scheme to apply BE to large molecular systems with comparable accuracy to other linear scaling electronic structure methods.[44]

Given the widespread success of these methods, developments have focused on improving their accuracy and applicability. As mentioned earlier, one source of error arises from the approximations applied to solve the system Hamiltonian and obtain the system wavefunction used for the Schmidt decomposition. Some work has been done in improving the initial system wavefunction, thus improving the approximate fragment-bath entanglement contained in the derived bath states. A vast majority of the literature uses RHF baths but bath states have also been derived from Kohn-Sham determinants,[23] Hartree-Fock-Bogoliubov determinants,[28] antisymmetrized geminal power functions,[26] and block product states.[31,38] Most of these developments used spin-restricted mean-field solutions, however a few works have explored spin-unrestricted solutions, namely UHF.[22,27] Ionization potentials (IP) and electron affinities (EA),[45,46] as well as spin-splittings and excited states in general,[47,48] are key properties that must be understood for the discovery and application of many catalytic and semiconductor materials, for example. It is known that spin-restricted mean-field methods are inadequate to accurately calculate these properties.[47] Moreover, studies have shown that correlated electronic structure methods provide significant improvement for these calculations when compared to non-correlated methods.[48] Given this, Schmidt decomposition based embedding methods could find much success in calculating IPs, EAs, and spin-splittings. However, these calculations are impossible without a spin-unrestricted bath and have never been done for molecules.

In this work, we seek to fill this void by adapting the BE method to start from a spin symmetry broken UHF solution, from which the fragment-bath entanglement can be approximated. We denote this method as unrestricted BE (UBE) as opposed to restricted BE (RBE), or BE starting from an RHF solution as in all previous works. We present here an implementation of UBE for molecules and demonstrate its use in computing IP/EA and excited state triplet energies in strongly correlated molecular systems.

This paper is organized as follows. Section II summarizes the theory required for UBE. We briefly review the Schmidt decomposition for unrestricted determinants, which has been covered in more detail in previous literature.[22,27] The BE procedure is also summarized, emphasizing key differences between UBE and RBE and the remaining details can be found in previous literature.[24] In Section III, we detail the H_{12} symmetric hydrogen ring system used for the calculations. We suspect UBE to be most applicable to strongly correlated systems and this system in a minimal basis serves as a model molecular system for this limit. In Section IV, we highlight the improved functionality of UBE calculations by computing the IP/EA and triplet energies of H_{12}, which were previously unattainable with RHF based Schmidt decomposition embedding methods. We also calculate the singlet energies of the neutral, dicationic, and dianionic species to contrast RBE and UBE. We compare our results against RBE (whenever possible) and unrestricted CC with single and double excitations (CCSD). We find that even for cases where RBE calculations are possible, UBE converges where RBE fails. Moreover, UBE consistently performs on par with CCSD. In Section V, we summarize our findings and discuss potential directions to improve UBE in terms of applicability and efficiency, many of which have already been implemented for DMET and RBE.

II. THEORY

The Schmidt decomposition of unrestricted determinants[22,27] and BE[24,25,42–44] have been covered in previous works and the reader should refer to those works for more detail. In this section, we provide a brief review of these elements. We emphasize differences between UBE and RBE.

A. Schmidt Decomposition for Unrestricted Determinants

For a chemical system we have the following Hamiltonian.

$$\hat{H} = \sum_{\sigma} \sum_{\mu\nu}^{N} h_{\mu\nu}^{\sigma} \hat{c}_{\mu}^{\sigma\dagger} \hat{c}_{\nu}^{\sigma} + \frac{1}{2} \sum_{\sigma\tau} \sum_{\mu\nu\lambda\eta}^{N} V_{\mu\nu\lambda\eta}^{\sigma\tau} \hat{c}_{\mu}^{\sigma\dagger} \hat{c}_{\lambda}^{\tau\dagger} \hat{c}_{\eta}^{\tau} \hat{c}_{\nu}^{\sigma} \quad (1)$$

where μ, ν, λ, η iterate over all N spatial orbitals and σ, τ iterate over α and β spins. $h_{\mu\nu}^{\sigma}$ and $V_{\mu\nu\lambda\eta}^{\sigma\tau}$ are the one and two electron integrals respectively. $\hat{c}_{\mu}^{\sigma\dagger}$ ($\hat{c}_{\mu}^{\sigma}$) is the creation (annihilation) operator for spatial orbital μ with spin σ.

The Schmidt decomposition[49] in the context of a site basis (such as local and orthonormal orbitals for molecules) allows us to take a Hilbert space divided into a fragment subspace (call it A) and corresponding bath subspace and write the system wavefunction, which can be any general wavefunction not limited to mean-field wavefunctions, as

$$|\Psi\rangle = \sum_{p=1}^{N^A} \lambda_p^A \left|f_p^A\right\rangle \otimes \left|b_p^A\right\rangle \quad (2)$$

where $\left|f_p^A\right\rangle$ are states that span the Hilbert space of the fragment, denoted as fragment states, and $\left|b_p^A\right\rangle$ are states

within the Hilbert space of the corresponding bath, denoted as bath states. The advantage of the Schmidt decomposition is that the sum only goes up to the smaller number between the number of fragment and bath states, which is usually the number of fragment states and we denote it N^A. Only states in the bath space with entanglement ($\lambda_p \neq 0, 1$) are kept in this decomposition.

Although the Schmidt decomposition can be applied to any state, the Schmidt decomposition for a correlated wavefunction must be written in terms of many electron states, which is a great computational burden. In the specific case of a mean-field determinant though, the states spanning the fragment and bath can be simplified from a many electron state to a set of one electron states derived from the mean field determinant.

Solving the full system Hamiltonian in Equation (1) at the UHF level yields the spin-unrestricted determinant $|\Psi_{\text{UHF}}\rangle$ with $N \times N$ coefficient matrices $\mathbf{C}^\alpha$ and $\mathbf{C}^\beta$ representing the transformation of the starting basis, in our case a set of orthonormal local orbitals (LOs) obtained from symmetrically orthogonalizing[56] the atomic orbitals, into the molecular orbitals (MOs) for each spin component. We can divide the coefficient matrices into an occupied and virtual component.

$$\mathbf{C}^\sigma = \left[\mathbf{C}^\sigma_{\text{occ}} \middle| \mathbf{C}^\sigma_{\text{vir}}\right] \tag{3}$$

In what follows, we will perform the Schmidt decomposition for a given fragment (call it A) on the occupied MOs. We partition our system of LOs into LOs which lie in A and LOs outside of A. The Schmidt decomposition finds a unitary rotation of all LOs such that there are at most N^A orbitals outside of A with non-zero overlap with the orbitals in A. Conceptually, although this unitary rotation does not affect the properties and observables of the wavefunction, it allows us to factorize the wavefunction into a part that includes the fragment and all orbitals with nonzero overlap and entanglement with the fragment and a part that is unentangled from the fragment. The philosophy behind Schmidt decomposition based methods is to recover correlation by performing a correlated calculation within the orbital space of first part.

In more detail, we define a partitioning A and we partition the occupied coefficient matrix for each spin component into the rows corresponding to LOs in A ($\mathbf{C}^{A\sigma}_{\text{occ;f}}$) and LOs outside of A ($\mathbf{C}^{A\sigma}_{\text{occ;b}}$).

$$\mathbf{C}^\sigma_{\text{occ}} = \begin{bmatrix} \mathbf{C}^{A\sigma}_{\text{occ;f}} \\ \mathbf{C}^{A\sigma}_{\text{occ;b}} \end{bmatrix} \tag{4}$$

The overlap or entanglement is measured through the singular value of these coefficient matrices. We perform a singular value decomposition on the occupied fragment and occupied bath component of the coefficient matrix to obtain

$$\begin{aligned} \mathbf{C}^{A\sigma}_{\text{occ;f}} &= \mathbf{U}^{A\sigma}_{\text{f}} \Sigma^{A\sigma}_{\text{f}} \mathbf{V}^{A\sigma T}_{\text{f}} \\ \mathbf{C}^{A\sigma}_{\text{occ;b}} &= \mathbf{U}^{A\sigma}_{\text{b}} \Sigma^{A\sigma}_{\text{b}} \mathbf{V}^{A\sigma T}_{\text{b}} \end{aligned} \tag{5}$$

For a UHF determinant, we can define the embedding basis as described in Equation (2) as

$$\begin{aligned} \left|f_p^{A\sigma}\right\rangle &= \sum_i^N U^{A\sigma}_{\text{f};ip} \left|\phi_i\right\rangle \\ \left|b_p^{A\sigma}\right\rangle &= \sum_i^N U^{A\sigma}_{\text{b};ip} \left|\phi_i\right\rangle \end{aligned} \tag{6}$$

where $\mathbf{U}^{A\sigma}_{\text{f}}$ and $\mathbf{U}^{A\sigma}_{\text{b}}$ are the left singular value decomposition matrices described in Equation (5) and $|\phi_i\rangle$ are the original LO basis. We refer to $\left|f_p^{A\sigma}\right\rangle$ as the fragment orbitals (FOs). Except for special cases,[42] there are N^A of $\left|b_p^{A\sigma}\right\rangle$ that have non-zero entanglement with the FOs and we refer these entangled states as the bath orbitals (BOs). The remaining orbitals with no entanglement with the FOs we refer to as environment orbitals (EOs) and we will denote them as $\left|e_p^{A\sigma}\right\rangle$ to distinguish them from the BOs. We will also distinguish the submatrix formed from the columns of $\mathbf{U}^{A\sigma}_{\text{b}}$ corresponding to the EOs as $\mathbf{U}^{A\sigma}_{\text{e}}$ ($\mathbf{U}^{A\sigma}_{\text{b}} \rightarrow [\mathbf{U}^{A\sigma}_{\text{b}} | \mathbf{U}^{A\sigma}_{\text{e}}]$).

The Schmidt decomposition of the UHF determinant for a given choice of fragment A is

$$|\Psi_{\text{UHF}}\rangle = \prod_\sigma \left[\sum_{p=1}^{N^A} \left(\lambda_p^A \left|f_p^{A\sigma}\right\rangle \otimes \left|b_p^{A\sigma}\right\rangle\right) \otimes \left|\Psi^{A\sigma}_{\text{core}}\right\rangle\right] \tag{7}$$

where the FOs, BOs, and EOs are as defined in Equation (6) and proceeding discussion. $\left|\Psi^{A\sigma}_{\text{core}}\right\rangle$ is the frozen core contribution formed from the remaining $2(N-2N^A)$ EOs.

The $2N^A$ combined FOs and BOs form an active space for our fragment with core contributions from the EOs. We write the fragment Hamiltonian for fragment A as

$$\begin{aligned} \hat{H}^A = &\sum_\sigma \sum_{pq}^{2N^A} h^{A\sigma}_{pq} \hat{a}_p^{A\sigma\dagger} \hat{a}_q^{A\sigma} \\ &+ \frac{1}{2} \sum_{\sigma\tau} \sum_{pqrs}^{2N^A} V^{A\sigma\tau}_{pqrs} \hat{a}_p^{A\sigma\dagger} \hat{a}_r^{A\tau\dagger} \hat{a}_s^{A\tau} \hat{a}_q^{A\sigma} \end{aligned} \tag{8}$$

where p, q, r, s index the FOs and BOs combined space and $\hat{a}_p^{A\sigma\dagger}$ ($a_p^{A\sigma}$) are the equivalent creation (annihilation) operators as in Equation (1) for FOs and BOs. $h^{A\sigma}_{pq}$ and $V^{A\sigma\tau}_{pqrs}$ are the one and two electron integrals in the embedding active space and have the form

$$h^{A\sigma}_{pq} = \sum_{\mu\nu}^N U^{A\sigma}_{\mu p} F^{A\sigma}_{\text{eff};\mu\nu} U^{A\sigma}_{\nu q} \tag{9}$$

$$V^{A\sigma\tau}_{pqrs} = \sum_{\mu\nu\lambda\eta}^N U^{A\sigma}_{\mu p} U^{A\sigma}_{\nu q} V_{\mu\nu\lambda\eta} U^{A\tau}_{\lambda r} U^{A\tau}_{\eta s} \tag{10}$$

where $\mathbf{U}^{A\sigma} = [\mathbf{U}_{\mathrm{f}}^{A\sigma}|\mathbf{U}_{\mathrm{b}}^{A\sigma}]$ is the transformation of the LO basis into the combined FO and BO basis. $\mathbf{F}_{\mathrm{eff}}^{A\sigma}$ is the effective fock matrix, which consists of the one electron interactions within the FOs/BOs space and the coulomb and exchange interactions between the FOs/BOs and the EOs. Equation (9) can be solved at different levels of theory including FCI,[24,25] MP2,[42,43] and CCSD.[44] In this work, the fragment Hamiltonian is solved using FCI.

B. Unrestricted Bootstrap Embedding

Embedding schemes based on the Schmidt decomposition involve a self-consistent matching condition to improve the accuracy of the fragment calculation. The original work on DMET sought to improve the mean-field wavefunction (and thus the accuracy of the entanglement it predicts to improve the FO and BO basis) by matching the mean-field wavefunction to the fragment wavefunctions by means of the density matrix[19,20] and later works by means of the density.[21,22] However, it would be ideal to match two correlated wavefunctions instead, which can achieve exact matching as there are cases that a mean-field wavefunction cannot match a correlated wavefunction.[24] Another aspect of embedding schemes is that the error of the fragment calculation lies mostly on the boundaries, where the interaction between the fragment and (low-level) bath is most strong.

The philosophy behind BE is to overcome both of these difficulties by partitioning the system into overlapping fragments. Each fragment is divided into a center subfragment, where the fragment-bath interactions are suspected to be weak, and an edge subfragment, where the fragment-bath interactions are suspected to be strong. The wavefunction on the edge subfragment, which is poorly captured by the fragment calculation, is constrained to match the wavefunction on those same sites but on a different, overlapping fragment where those sites are considered part of the center subfragment. The matching is done through constraining the density matrix elements in BE. This philosophy is illustrated in Figure 1.

Previous works on BE have started from an RHF solution. This work will start from a UHF solution using the procedure described in Section II A to obtain each fragment Hamiltonian. The detailed methodology[24,25,42] including special cases of RBE[43,44] has been described in previous literature so this paper will focus on the UBE matching condition, which are more nuanced than the RBE conditions because of spin symmetry breaking.

We define the fragment one particle density matrix (1PDM) and two particle density matrix (2PDM) in the embedding basis for fragment A as

$$P_{pq}^{\sigma A} = \left\langle \hat{a}_p^{A\sigma\dagger} \hat{a}_q^{A\sigma} \right\rangle_A \tag{11}$$

$$\Gamma_{pqrs}^{\sigma\tau A} = \left\langle \hat{a}_p^{A\sigma\dagger} \hat{a}_r^{A\tau\dagger} \hat{a}_s^{A\tau} \hat{a}_q^{A\sigma} \right\rangle_A \tag{12}$$

For a fragment A, we partition the fragment into two

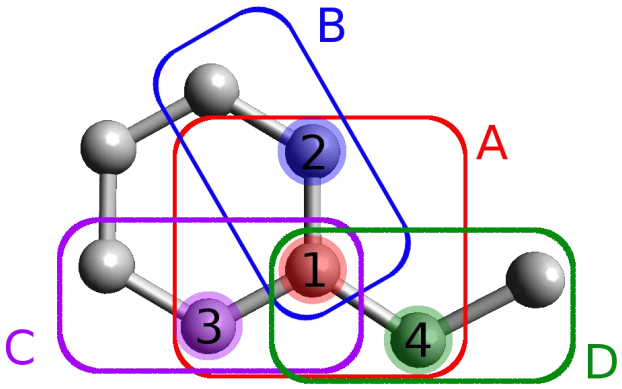

FIG. 1: An illustration of the BE matching philosophy. Four fragments are pictured here by a box encapsulating the sites contained in the fragment and the highlighted site with the same color is considered the center of the fragment. Fragment A contains sites 1, 2, 3, and 4 where the center of A contains only 1 and the edge of A contains 2, 3, and 4. The wavefunction of fragment A is constrained so that the wavefunction on site 2 agrees with the wavefunction of fragment B on site 2, the wavefunction on site 3 agrees with the wavefunction of fragment C on site 3, and the wavefunction on site 4 agrees with the wavefunction of fragment D on site 4. Similarly, site 1 is contained in the the center of fragment A and the edge of all other fragments, so the wavefuntion of fragment B, C, and D is constrained so that their wavefunctions on site 1 agrees with the wavefunction of fragment A on site 1, among other constraints.

disjoint subfragments. Let $\mathbb{C}^A$ denote the center subfragment and let $\mathbb{E}^A$ denote the edge subfragment of A. For simplicity, we consider the case where the center subfragments of different fragments do not overlap. Other cases have been detailed in previous works.[43] The fragment calculation has two constraints. The first condition in RBE is a local constraint to enforce that the 1PDM elements corresponding to the inaccurate edge sides matches the 1PDM of the more accurate center sites (as described in the caption to Figure 1). The RBE condition is simply

$$\left\langle \hat{a}_p^{A\dagger} \hat{a}_q^{A} \right\rangle_A = P_{pq}^B \tag{13}$$

for all fragments $B \neq A$ where p and q are the edge site of fragment A and center site of fragment B. Every fragment calculation is further constrained by a global constraint to enforce that the total number of electrons remains consistent. For RBE, this is simply enforcing that

$$\sum_A \sum_{p \in \mathbb{C}^A} \left\langle \hat{a}_p^{A\dagger} \hat{a}_p^{A} \right\rangle_A = N_e \tag{14}$$

These conditions require additional care in UBE because spin dependent expectation values are obtained fol-

lowing the procedure for starting from a UHF determinant described in Section II A. In particular, we have spin dependent 1PDMs. Regarding the local constraint in Equation (13), we have a choice between matching our density matrices in a spin dependent way where each spin component is matched separately ($\langle \hat{a}_p^{A\sigma\dagger} \hat{a}_q^{A\sigma} \rangle_A = P_{pq}^{\sigma B}$) or a spin independent way where the sum of the spin components is matched ($\langle \hat{a}_p^{A\alpha\dagger} \hat{a}_q^{A\alpha} + \hat{a}_p^{A\beta\dagger} \hat{a}_q^{A\beta} \rangle_A = P_{pq}^{\alpha B} + P_{pq}^{\beta B}$). We choose to enforce a spin independent matching for this constraint.

$$\min_{\Psi^A} \left\langle \hat{H}^A \right\rangle_A \text{ s.t. } \forall B \neq A, \forall p,q \in \mathbb{E}^A \cap \mathbb{C}^B \\ \left\langle \hat{a}_p^{A\alpha\dagger} \hat{a}_q^{A\alpha} + \hat{a}_p^{A\beta\dagger} \hat{a}_q^{A\beta} \right\rangle_A = P_{pq}^B \tag{15}$$

where $\mathbf{P}^B = \mathbf{P}^{\alpha B} + \mathbf{P}^{\beta B}$ is the spin-summed 1PDM. The reason for this choice is because for spin-unrestricted calculations, the spin symmetry breaking can be "artifactual," meaning the symmetry breaking is an artifact of the approximation and bears no physical meaning. Hence, any spin symmetry breaking in the fragment is equivalently artifactual. Approximations that lead to spin symmetry breaking have been studied intensively in systems such as fullerenes where it was found that UHF resulted in spin symmetry breaking not related to strong correlation.[50,51] Moreover, significant spin symmetry breaking will be required, artifactual or not, in systems with strong correlation and UHF can result in significant spin contamination. Because of both of these reasons, it would go against the philosophy of UBE, where the fragment wavefunction is improved through matching to a nearly exact wavefunction, to match the fragment wavefunction in a spin dependent sense to another wavefunction that can have artifactual and unphysical spin symmetry breaking.

UBE again requires a choice between a spin dependent or spin independent matching for the global constrain in Equation (14). However, this case is simple and we choose to match the total number of electrons in a spin dependent way. Although the spin symmetry breaking can be artifactual, the number of α and β electrons is well-defined. The global constraint is as follows.

$$\sum_A \sum_{p \in \mathbb{C}^A} \left\langle \hat{a}_p^{A\alpha\dagger} \hat{a}_p^{A\alpha} \right\rangle_A = N_e^\alpha \\ \sum_A \sum_{p \in \mathbb{C}^A} \left\langle \hat{a}_p^{A\beta\dagger} \hat{a}_p^{A\beta} \right\rangle_A = N_e^\beta \tag{16}$$

where N_e^α and N_e^β denotes the total number α and β electrons in the full system.

Equations (15) and (16) lead to the following Lagrangian.

$$\mathcal{L} = \sum_A^{N_{\text{frag}}} \Bigg[\left\langle \hat{H}^A \right\rangle_A - \mathcal{E}^A \left(\langle \hat{1} \rangle_A - 1 \right) + \\ \sum_{B \neq A}^{N_{\text{frag}}} \sum_{pq \in \mathbb{E}^A \cap \mathbb{C}^B} \lambda_{pq}^A \Big(\left\langle \hat{a}_p^{A\alpha\dagger} \hat{a}_q^{A\alpha} + \hat{a}_p^{A\beta\dagger} \hat{a}_q^{A\beta} \right\rangle_A \\ - P_{pq}^B \Big) \Bigg] + \\ \mu^\alpha \Bigg[\left(\sum_A^{N_{\text{frag}}} \sum_{p \in \mathbb{C}^A} \left\langle \hat{a}_p^{A\alpha\dagger} \hat{a}_p^{A\alpha} \right\rangle_A \right) - N_e^\alpha \Bigg] + \\ \mu^\beta \Bigg[\left(\sum_A^{N_{\text{frag}}} \sum_{p \in \mathbb{C}^A} \left\langle \hat{a}_p^{A\beta\dagger} \hat{a}_p^{A\beta} \right\rangle_A \right) - N_e^\beta \Bigg] \tag{17}$$

where $\{\lambda_{pq}^A\}$ are the Lagrange multipliers to enforce Equation (15) and μ^α and μ^β are the two Lagrange multipliers to enforce the two conditions in Equation (16). N_{frag} is the number of fragments. Solving for the stationary point of Equation (17) with respect to Ψ^A leads to the following eigenvalue equation.

$$\left[\hat{H}^A + \sum_{pq \in \mathbb{E}^A} \lambda_{pq}^A \left(\hat{a}_p^{A\alpha\dagger} \hat{a}_q^{A\alpha} + \hat{a}_p^{A\beta\dagger} \hat{a}_q^{A\beta} \right) + \mu^\alpha \sum_{p \in \mathbb{C}^A} \hat{a}_p^{A\alpha\dagger} \hat{a}_p^{A\alpha} + \mu^\beta \sum_{p \in \mathbb{C}^A} \hat{a}_p^{A\beta\dagger} \hat{a}_p^{A\beta} \right] \left| \Psi^A \right\rangle = \mathcal{E}^A \left| \Psi^A \right\rangle \tag{18}$$

This yields a new effective fragment Hamiltonian. The previous fragment Hamiltonian in Equation (8) is now dressed with a local effective potential, λ_{pq}^A, and global chemical potentials, μ^σ.

Equation (18) can be solved for each fragment, but the problem is that each fragment Hamiltonian is highly coupled to other fragment Hamiltonians. The target densities (P_{pq}^B), and thus λ_{pq}^A and μ^σ, depend on the solution to Equation (18) for all fragments B with a matching condition for the fragment of interest. To decouple these equations, we adopt the same iterative process used in RBE.[42,43] We consider two loss functions

$$L_\lambda^A(\lambda^A) = \\ \left[\frac{1}{N_{\text{cons}}} \sum_A^{N_{\text{frag}}} \sum_{B \neq A}^{N_{\text{frag}}} \sum_{pq \in \mathbb{E}^A \cap \mathbb{C}^B} \left(P_{pq}^A(\lambda^A) - P_{pq}^B \right)^2 \right]^{\frac{1}{2}} \tag{19}$$

$$L_\mu^\sigma(\mu^\alpha, \mu^\beta) = \left[\sum_A^{N_{\text{frag}}} \sum_{p \in \mathbb{C}^A} P_{pp}^{\sigma A}(\mu^\alpha, \mu^\beta) \right] - N_e^\sigma \tag{20}$$

where N_{cons} is the number of 1PDM constraints. Although the target densities we are matching to, P^B_{pq} in Equation (19), also depend on the local effective potentials λ^B, we temporarily fix the target densities and optimize the local effective potential on each fragment for the fixed target densities. The target densities are updated with the new local effective potential in the next iteration. Enforcing $L^\sigma_\mu = 0$ from Equation (20) defines a system of two equations (for each spin) of two variables which can be solved for both μ^α and μ^β simultaneously. Hence, Equation (19) is solved for $L^A_\lambda(\lambda^A) = 0$ in this decoupled manner for each fragment, then the target densities are updated using the converged effective potential. Finally, Equation (20) is solved for $L_\mu(\mu^\alpha, \mu^\beta) = 0$ with respect to μ^α and μ^β simultaneously to obtain the global chemical potential. These steps are repeated until L^A_λ, L^α_μ, and L^β_μ are all below a tolerance.

We note that the local effective potential defined by Equation (19) accounts for the philosophy described earlier in this section and in Figure 1. This potential distinguishes BE from a simple local active space calculation based on the Schmidt decomposition. Therefore, in order to assess the effectiveness of the BE philosophy, we develop an alternative, simplified prescription to regular BE. In this modification, we fix the local effective potential to zero, $\lambda^A = 0$, for all fragments effectively removing the 1PDM matching constraint in Equation (15). Only Equation (19) is solved for $L_\mu = 0$ to obtain the global chemical potential, μ^σ. When the fragment calculation is simplified in this manner, we call the calculation one-shot BE or BE0, and use RBE0 and UBE0 to denote whether a spin-restricted or spin-unrestricted bath is used. The difference between the BE and BE0 calculation provides a quantitative measure of how the unique BE matching philosophy, expressed through the 1PDM matching constraints, affects the embedding calculation.

After the potentials are converged, we can calculate the UBE(0) energy with an expression similar to the RBE energy.

$$\begin{aligned} E_{\text{UBE}} = &\sum_A^{N_{\text{frag}}} \sum_{p\in\mathbb{C}^A} \\ &\Bigg[\sum_\sigma \sum_q^{2N^A} \left(h^{A\sigma}_{pq} + \frac{1}{2} G^{A\sigma}_{\text{core};pq}\right) P^{\sigma A}_{pq} \\ &+ \sum_\sigma \sum_{qrs}^{2N^A} V^{A\sigma\sigma}_{pqrs} \Gamma^{\sigma\sigma A}_{pqrs} + \\ &\frac{1}{2} \sum_{qrs}^{2N^A} \left(V^{A\alpha\beta}_{pqrs} \Gamma^{\alpha\beta A}_{pqrs} + V^{A\beta\alpha}_{pqrs} \Gamma^{\beta\alpha A}_{pqrs}\right)\Bigg] \end{aligned} \tag{21}$$

where $\mathbf{G}^{A\sigma}_{\text{core}}$ is the coulomb minus the exchange interaction between the FOs/BOs and EOs.

III. COMPUTATIONAL DETAILS

All UBE(0) and RBE(0) calculations were done on in-house software which takes electron integrals from alternative software as an input and utilizes the Eigen library for matrix algebra.[52] Full CI (FCI)[7] is used as the fragment solver to solve Equation (18). The optimization of Equations (19) and (20) were done using Newton's method with numerical derivatives. Electron integrals were evaluated using PySCF.[53] We compare UBE results against unrestricted CCSD calculations (CCSD starting from an unrestricted reference)[54] and FCI results, both also calculated using PySCF.

Integrals were computed in a STO-3G basis set[55] with Löwdin symmetric orthogonalization.[56] It has been discussed in detail in previous works[43] that Schmidt decomposition based embedding schemes do a poor job of recovering dynamic correlation and should be regarded as a generalization to complete active space (CAS) methods.[57–59] For the purpose of testing UBE as a strong correlation method, a minimal basis is sufficient.

The system used in this paper a symmetric ring of twelve hydrogen atoms. The energy of the system is calculated as the distance between each hydrogen atom is varied, resulting in a symmetric ring expansion. This distance is denoted r in further discussions. The geometry of this system is pictured in Figure 2. For each different set of calculations, we vary the number of α and β electrons in this system. We study two specific cases in particular, systems with $N^\alpha_e = N^\beta_e$ and $M_S = 0$ and systems where $N^\alpha_e \neq N^\beta_e$. The first case allows an RHF, and thus an RBE, calculation to compare against. The XYZ data for each geometry used in this work can be found in the Supplementary Material. Furthermore, we divide the system into twelve overlapping fragments, each with three hydrogen atoms. For each fragment, a unique hydrogen atom is taken as the center and the edges are taken as the two nearest hydrogen atoms. A few sample fragments are also pictured in Figure 2. We choose a smaller fragment size so that exact FCI calculations can be done in the fragment space. Moreover, our goal is to compare and contrast UBE and RBE. The distinct advantage of UBE to be presented lies in its versatility over RBE, and a small fragment size demonstrates this adequately. The procedure for larger sites would be easy to implement and has been done for similar systems to successfully improve accuracy in previous works.[24,25] Should the accuracy, which will be seen to be quite good already, be the focus in future works, then the accuracy can trivially be improved by increasing the fragment size.

In the following section, UBE, UBE0, RBE (when possible), RBE0 (when possible), and unrestricted CCSD calculations are ran at each geometry and plotted against the FCI energy. We refer to the energy error as the energy calculated from the method in question subtracted from the FCI energy. In the Supplementary Material, we include plots of the total energy of these methods, along with the total energy of RHF (when possible), UHF, and

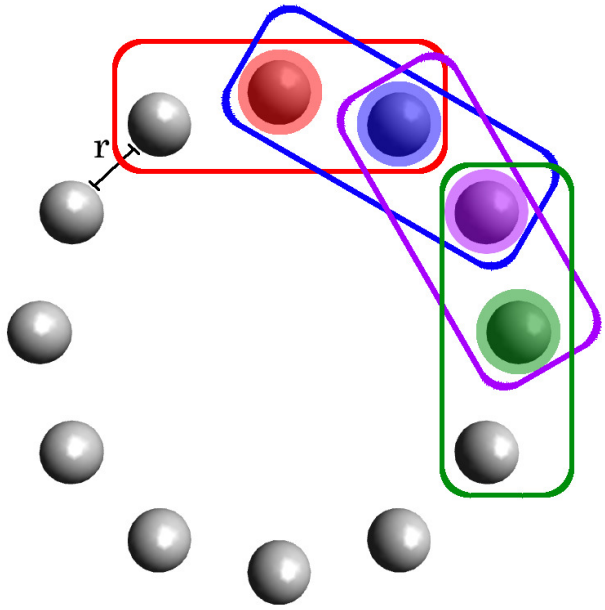

FIG. 2: Geometry of the H_{12} symmetric ring system and our fragmenting scheme. All hydrogens are arranged equidistant from the adjacent hydrogens in a ring. The distance between neighboring hydrogens, r, is varied, leading to a symmetric ring expansion. Four sample fragments are pictured here to illustrate our fragmenting scheme. Each box outlines a fragment and the highlighted atom with the same color denotes the center subfragment.

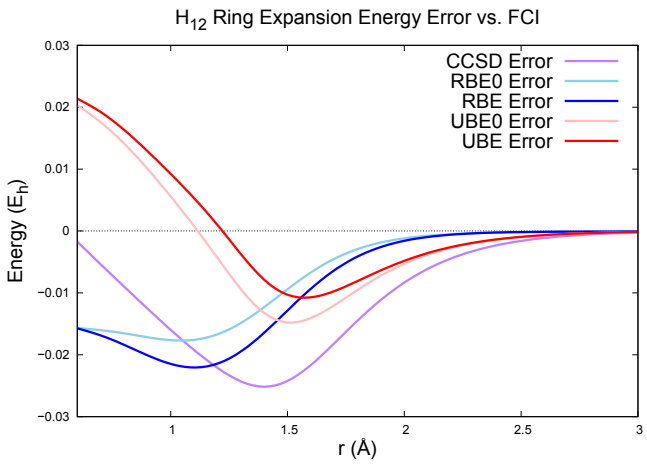

FIG. 3: H_{12} symmetric ring expansion energy error for UBE (red), UBE0 (light red), RBE (blue), RBE0 (light blue), and unrestricted CCSD (purple).

FCI calculations for each species.

IV. RESULTS

A. Strong Correlation

We begin our analysis by studying the neutral species, the dication, and the dianion, where we can obtain an RBE solution to compare against. It is well known that RHF fails in predicting accurate energies in the large r limit compared to UHF. Hence, it is an interesting question in these cases as to whether or not UBE does significantly better than RBE.

The energy errors of all the stated methods for neutral H_{12} are plotted in Figure 3. We find that in general, all these methods are highly accurate and perform comparably. We see that both UBE and RBE perform better in the large r limit than CCSD, whereas there is no clear winner in the small r limit. It is interesting that not only does RBE out perform UBE in the large r limit, but that RBE0 outperforms RBE consistently. The first point is surprising because UHF provides a better wavefunction in terms of 1PDM and energy. However, because of the smaller overlap between the UHF wavefunction and FCI wavefunction compared to the RHF wavefunction, it is possible that the Schmidt decomposition of the UHF wavefunction does not accurately captures fragment-bath entanglement in this case. In this vein of thought, one way UHF falls short of RHF compared to FCI is in terms of electron localization. RHF and FCI both predict uniform localization whereas UHF predicts unphysical, nonuniform localization. A plot of the Mulliken population[60] on each hydrogen atom can be found in the Supplementary Material. Regarding the second point about RBE0's surprising performance, we do not have an explanation and suspect this to be a case of cancellation of errors. Both of these behaviors are not repeated for our next systems.

The energy errors for H_{12}^{2+} and H_{12}^{2-} are plotted in Figure 4. Similar to the result for the neutral species, UBE, RBE, and unrestricted CCSD perform comparably for both the dication and dianion species. The improvement of RBE and UBE over RBE0 and UBE0, respectively, demonstrates the need for the 1PDM matching constraint. We find that the RBE algorithm does not converge past 2.00 Å. The optimization of Equation (19) for the inter-system 1PDM matching constraint diverges. We suspect the reason for this instability arises from the poor quality of the RHF state, and this problem does not occur for UBE. In summary, UBE improves upon the functionality of RBE by converging for cases where RBE does not converge and performs similarly where both methods converge.

B. IP/EA Calculations

Our next analysis will focus on doublet electronic states. This is a case that RBE is incapable of modeling and UBE is necessary over RBE. In particular, we will study the cation and anion species of H_{12} and compute

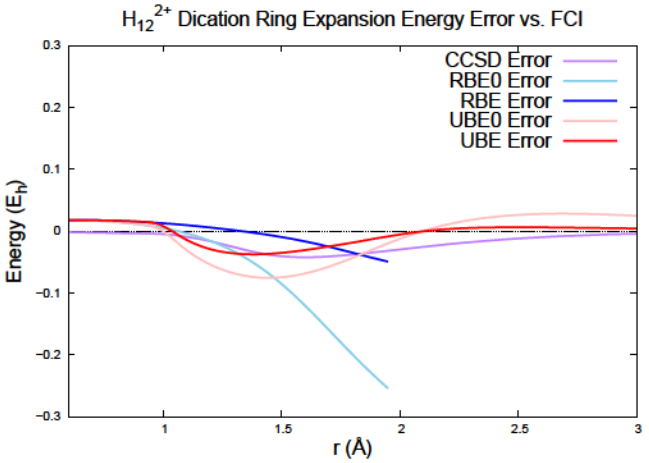

(a) H_{12}^{2+} dication symmetric ring expansion energy error for UBE (red), UBE0 (light red), RBE (blue), RBE0 (light blue), and unrestricted CCSD (purple).

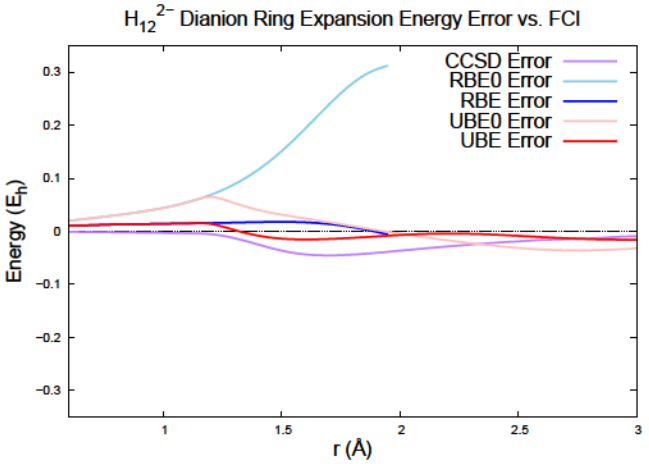

(b) H_{12}^{2} dianion symmetric ring expansion energy error for UBE (red), UBE0 (light red), RBE (blue), RBE0 (light blue), and unrestricted CCSD (purple).

FIG. 4: H_{12}^{2+} dication and H_{12}^{2-} dianion energy errors.

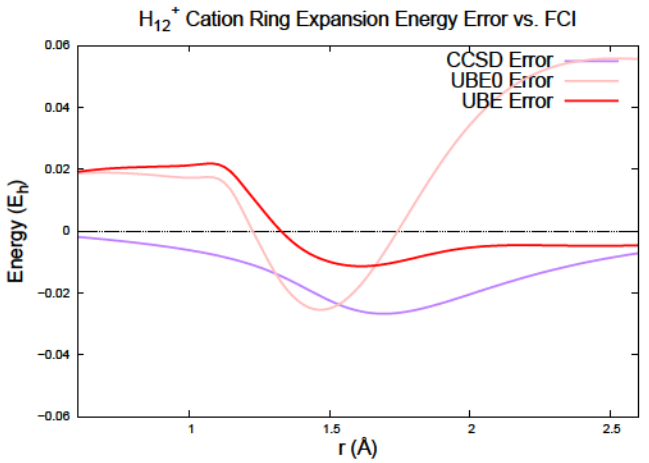

(a) H_{12}^{+} cation symmetric ring expansion energy errors for UBE (red), UBE0 (light red), and unrestricted CCSD (purple).

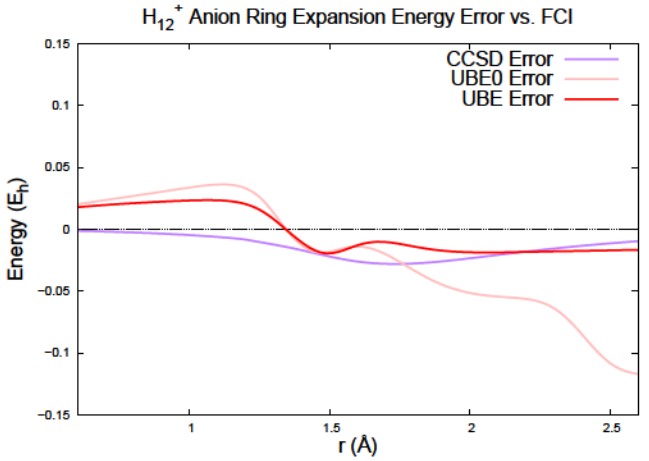

(b) H_{12} anion symmetric ring expansion energy errors for UBE (red), UBE0 (light red), and unrestricted CCSD (purple).

FIG. 5: H_{12}^{+} cation and H_{12}^{-} anion energy errors.

the IPs and EAs of H_{12}.

The energy errors for H_{12}^{+} and H_{12}^{-} are plotted in Figure 5. We see similar behavior in both figures. UBE improves significantly over UBE0 when the error of UBE0 grows greater than $\sim$0.02 E_h. The matching condition does its job in keeping the error low. Similar to the results in Section IV A, unrestricted CCSD does exceptionally well in the small r limit and is comparable to UBE in the large r limit. The error in general for both UBE and unrestricted CCSD remains quite small and both methods seem to comparably reproduce the FCI energy.

In chemistry, we are typically more concerned with energy differences than absolute energies, so we turn our attention to the IP (E(cation) $-$ E(neutral)) and EA (E(neutral) $-$ E(anion)) of H_{12}. In Figure 6, we plot the IP and EA errors for UBE and CCSD against the FCI IP and EA. In general, it is fair to say that UBE and unrestricted CCSD perform similarly. UBE does well in the small r and large r extremes. It is interesting to note that although CCSD outperforms UBE in the small r limit for the neutral and ionic species, the error cancellation is on UBE's side at this limit. The greatest errors happen in the recoupling region between these two limits (approximately 1.00 Å to 1.20 Å), where the spin angular momentum of the UHF wavefunction changes most rapidly. This indicates that something complex is happening in this mid-range. One observation is a sudden, nonuniform electron localization predicted by the UHF wavefunction starting in this region. The FCI wavefunction predicts a much more uniform electron localization. This population analysis can be found in the Supplementary Material. Though this irregularity is likely due to the high symmetry of the system and may not necessarily indicate a recoupling region for systems with less symmetry, this

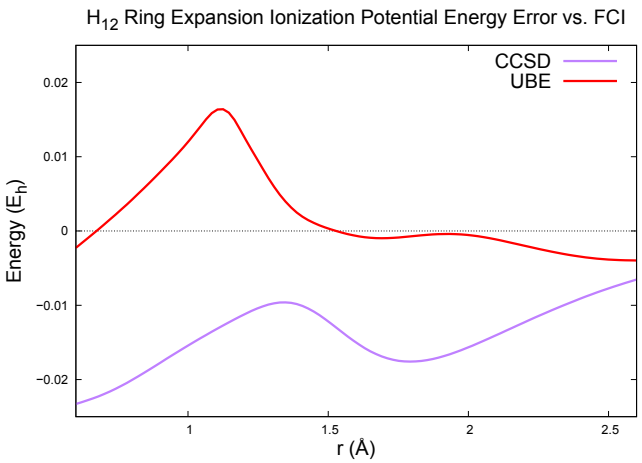

(a) H_{12} symmetric ring expansion IP errors for UBE (red), UBE0 (light red), and unrestricted CCSD (purple).

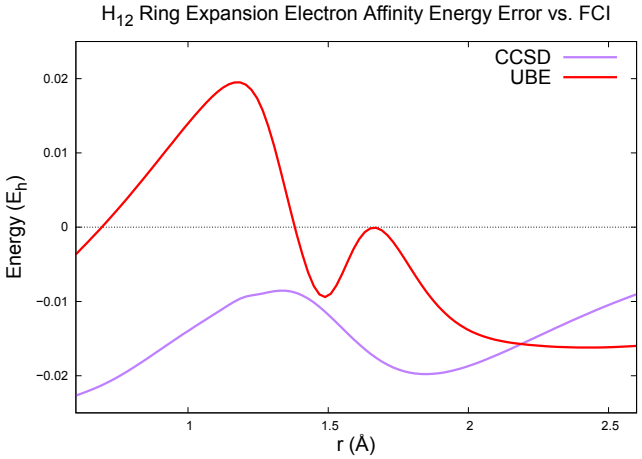

(b) H_{12} symmetric ring expansion EA errors for UBE (red), UBE0 (light red), and unrestricted CCSD (purple).

FIG. 6: H_{12} symmetric ring expansion IP and EA errors.

occurrence highlights that the initial UHF state can be highly erroneous without further optimization. One aspect of BE that has not been explored in either RBE or UBE is the fact that the full system state is optimized once at the beginning and never again. In DMET, this state is re-optimized in a self-consistent algorithm.[36] It will be interesting for future works to see if orbital re-optimization for UBE's initial UHF state can help improve the IP and EA calculations in this recoupling region where the spin symmetry of the UHF wavefunction is most unstable. Regardless, UBE has proven capable of unrestricted CCSD accuracy for IP and EA calculations out of reach of RBE.

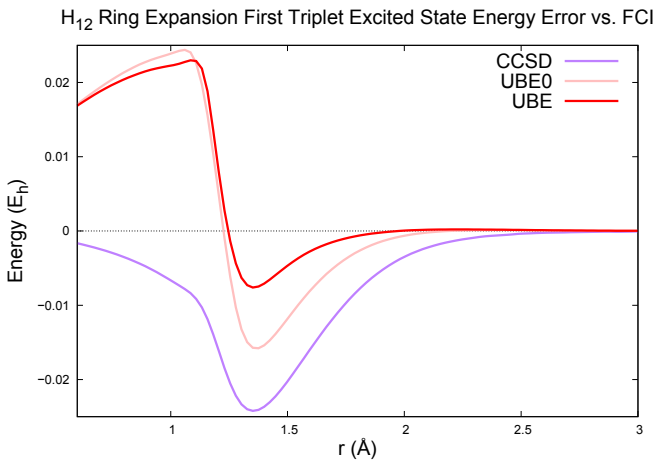

FIG. 7: H_{12} symmetric ring expansion first triplet excited state energy errors for UBE (red), UBE0 (light red), and unrestricted CCSD (purple).

C. Triplet State Calculation

The last case in this work is the first triplet excited state for H_{12}, another state out of reach of RBE. We run the UBE and unrestricted CCSD with $N_e^\alpha = 7$ and $N_e^\beta = 5$.

Figure 7 plots the energy errors for the first triplet excited state of H_{12}. The same observations for the other systems apply here too. First, unrestricted CCSD out performs UBE in the small r limit and UBE outperforms CCSD in the large r limit. Regardless, the errors for both methods are remain small and comparable over the whole curve. Second, the matching condition has a positive impact on the UBE solution. There is either significant improvement or only very slightly deterioration (in the range approximately between 1.00 Å and 1.20 Å) going from UBE0 to UBE. The biggest concern is once again, the region between the small and large r limit. UBE switches from underestimating to overestimating the FCI energy and shows slightly worse energies compared to UBE0. This instability causes problems in the singlet-triplet gap as we will see in the proceeding discussion.

Finally, the singlet-triplet gap energy errors versus FCI for UBE and unrestricted CCSD are plotted in Figure 8. We see that UBE and unrestricted CCSD, again, perform comparably. The errors are similar in both magnitude and sign. It is interesting to note that UBE has performed noticeably better than unrestricted CCSD in the large r limit for the singlet and triplet state, but the error cancellation works out in favor of unrestricted CCSD and both methods have nearly the same error in this limit for the gap. Although the errors are similar for the rest of the curve, it is clear that UBE has the worse maximum error. This error happens in the recoupling region between 1.00 Å and 1.20 Å. This was discussed as a potential issue for the anion and cation species in Section IV B, and it seems to also be an issue for the

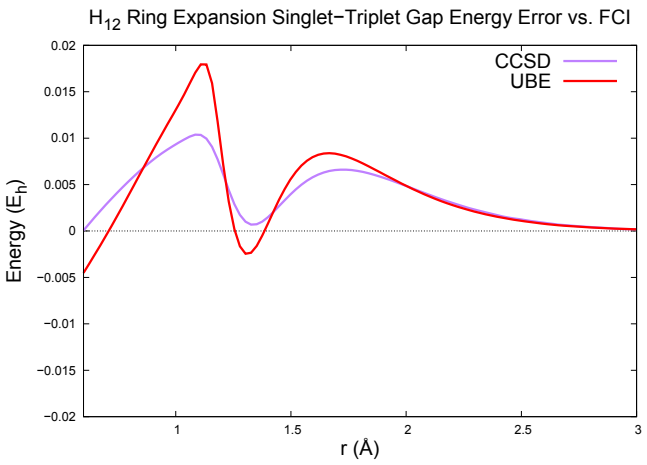

FIG. 8: H_{12} symmetric ring expansion singlet-triplet gap errors for UBE (red), UBE0 (light red), and unrestricted CCSD (purple).

triplet state of the neutral species. Again, orbital re-optimization is a possible solution. For our present data, we show that spin splittings comparable to unrestricted CCSD are possible with UBE, unlike RBE, but we also acknowledge that UBE is less consistent.

V. CONCLUSION

In this work we demonstrate that BE can be naturally extended to open shell systems using an unrestricted mean-field bath. When applied to model H_{12} examples, we find that—even with the smallest fragment sizes—UBE is of comparable accuracy to unrestricted CCSD. With the overall greater flexibility of UBE, we were able to calculate IPs/EAs and spin-splittings with CCSD accuracy for a strongly correlated system, something RBE has never been able to do.

Future work would benefit a lot from applying some of the same improvements RBE has seen to UBE. RBE has been successfully applied to molecules[42] in a black-box manner using Møller-Plesset second order perturbation theory (MP2)[61] and CCSD[44] as the fragment Hamiltonian solver. RBE has been efficiently implemented on molecular systems of a few thousand basis functions as accurately and as efficiently as modern linear scaling correlation methods.[44] All of these advances can now be directly combined with the advantages of UBE to access open shell and closed shell systems on the same footing.

In the vein of improving UBE itself, we reiterate that this study was limited to minimally sized fragments in order to focus on the improved versatility of UBE over RBE. RBE has demonstrated exponential convergence to the correct correlation energy with respect to fragment size.[24,43] Given than the smallest possible fragment size for UBE was already as successful as unrestricted CCSD, exploring larger fragment sizes is a simple, but promising direction.

Another intriguing direction for UBE is its application to electronic excited states. Fast scaling Schmidt decomposition embedding methods for excited states is still a relatively unexplored area except for a few discussions on DMET spectral functions[30,31,38,39] and an initial attempt to utilize higher lying RHF solutions as full system states to target excited states with DMET.[40] Most excited states with are impossible to model using RHF because they are open-shell in character, but UHF and related spin symmetry broken methods have had much more success.[62–65] UBE may be able to target more complicated excited states previously out of reach of RHF based DMET almost trivially by simply starting from these excited state UHF solutions. We have already demonstrated that UBE is capable of targeting the first triplet excited state.

This work also exposes some shortcomings of UBE. In particular, we find that UBE performs poorly in the mid-region where spin symmetry changes most dramatically. Future work should focus on overcoming this instability. One means we have suggested is to re-optimize the orbitals of the full system state on which the Schmidt decomposition is performed, something that is already done in DMET.[36]

In conclusion, the landscape of higher spin symmetry and open shell molecular species are now within reach of BE based methods. Future work utilizing prior advancements in RBE will allow UBE to study even larger systems of this nature.

VI. SUPPLEMENTARY MATERIAL

The Supplementary Materian includes all geometries used in this work, the final fragment 1PDMs of each RBE and UBE calculation in Section IV, the total energy curves for each calculation in Section IV, results for an alternative coordinate, and a Mulliken population analysis for each charged species.

VII. ACKNOWLEDGMENTS

This work was supported by a grant from the NSF (Grant No. CHE-1900358). HKT is an NSF Graduate Research Fellow.

VIII. DATA AVAILABILITY

All geometries used in this work and final fragment 1PDMs of each RBE and UBE calculation in Section IV are included in the Supplementary Material. Any additional data that supports the findings of this study are available from the corresponding author upon reasonable request.

[1] C. C. J. Roothaan, "New Developments in Molecular Orbital Theory," Rev. Mod. Phys. **23**, 69–89 (1951).

[2] C. C. J. Roothaan, "Self-consistent field theory for open shells of electronic systems," Rev. Mod. Phys. **32**, 179–185 (1960).

[3] P. Hohenberg and W. Kohn, "Inhomogeneous Electron Gas," Phys. Rev. **136**, B864 (1964).

[4] W. Kohn and L. Sham, "Self-Consistent Equations Including Exchange and Correlation Effects," Phys. Rev. **140**, A1133 (1965).

[5] M. J. MacLeod, A. J. Goodman, H.-Z. Ye, H. V.-T. Nguyen, T. Van Voorhis, and J. A. Johnson, "Robust gold nanorods stabilized by bidentate n-heterocyclic-carbene–thiolate ligands," Nature Chem **11**, 57–63 (2019), https://doi.org/10.1038/s41557-018-0159-8.

[6] C. A. Gaggioli, S. J. Stoneburner, C. J. Cramer, and L. Gagliardi, "Beyond density functional theory: The multiconfigurational approach to model heterogeneous catalysis," ACS Catalysis **9**, 8481–8502 (2019), https://doi.org/10.1021/acscatal.9b01775.

[7] I. Shavitt, "The history and evoluton of configuration interaction," Mol. Phys. **94**, 3–17 (1998).

[8] R. J. Bartlett and M. Musial, "Coupled-Cluster Theory in Quantum Chemistry," Rev. Mod. Phys. **79**, 291 (2007).

[9] J. F. Stanton and R. J. Bartlett, "The equation of motion coupled-cluster method. a systematic biorthogonal approach to molecular excitation energies, transition probabilities and excited state properties," J. Chem. Phys. **98**, 7029 (1993).

[10] M. L. Vidal, X. Feng, E. Epifanovsky, A. I. Krylov, and S. Coriani, "New and efficient equation-of-motion coupled-cluster framework for core-excited and core-ionized states," Journal of Chemical Theory and Computation **15**, 3117–3133 (2019), pMID: 30964297, https://doi.org/10.1021/acs.jctc.9b00039.

[11] J. McClain, Q. Sun, G. K.-L. Chan, and T. C. Berkelbach, "Gaussian-based coupled-cluster theory for the ground-state and band structure of solids," Journal of Chemical Theory and Computation **13**, 1209–1218 (2017), pMID: 28218843, https://doi.org/10.1021/acs.jctc.7b00049.

[12] F. R. Manby, M. Stella, J. D. Goodpaster, and T. F. Miller, "A simple, exact density-functional-theory embedding scheme," Journal of Chemical Theory and Computation **8**, 2564–2568 (2012), pMID: 22904692, https://doi.org/10.1021/ct300544e.

[13] D. V. Chulhai and J. D. Goodpaster, "Projection-based correlated wave function in density functional theory embedding for periodic systems," Journal of Chemical Theory and Computation **14**, 1928–1942 (2018), pMID: 29494155, https://doi.org/10.1021/acs.jctc.7b01154.

[14] X. Wen, D. S. Graham, D. V. Chulhai, and J. D. Goodpaster, "Absolutely localized projection-based embedding for excited states," Journal of Chemical Theory and Computation **16**, 385–398 (2020), pMID: 31769981, https://doi.org/10.1021/acs.jctc.9b00959.

[15] A. Severo Pereira Gomes and C. R. Jacob, "Quantum-chemical embedding methods for treating local electronic excitations in complex chemical systems," Annu. Rep. Prog. Chem., Sect. C: Phys. Chem. **108**, 222–277 (2012).

[16] C. R. Jacob and J. Neugebauer, "Subsystem density-functional theory," WIREs Computational Molecular Science **4**, 325–362 (2014), https://onlinelibrary.wiley.com/doi/pdf/10.1002/wcms.1175.

[17] T. A. Wesolowski, S. Shedge, and X. Zhou, "Frozen-density embedding strategy for multilevel simulations of electronic structure," Chemical Reviews **115**, 5891–5928 (2015), pMID: 25923542, https://doi.org/10.1021/cr500502v.

[18] I. Peschel and V. Eisler, "Reduced density matrices and entanglement entropy in free lattice models," J. Phys. A: Math. Theor. **42**, 504003 (2009).

[19] G. Knizia and G. K.-L. Chan, "Density Matrix Embedding: A Simple Alternative to Dynamical Mean-Field Theory," Phys. Rev. Lett. **109**, 186404 (2012).

[20] G. Knizia and G. K.-L. Chan, "Density Matrix Embedding: A Strong-Coupling Quantum Embedding Theory," J. Chem. Theory Comput. **9**, 1428–1432 (2013).

[21] I. W. Bulik, W. Chen, and G. E. Scuseria, "Intermediate and spin-liquid phase of the half-filled honeycomb Hubbard model," J. Chem. Phys. **141**, 054113 (2014).

[22] I. W. Bulik, G. E. Scuseria, and J. Dukelsky, "Density matrix embedding from broken symmetry lattice mean fields," Phys. Rev. B **89**, 035140 (2014).

[23] B. Senjean, "Projected site-occupation embedding theory," Phys. Rev. B **100**, 035136 (2019).

[24] M. Welborn, T. Tsuchimochi, and T. Van Voorhis, "Bootstrap embedding: An internally consistent fragment-based method," J. Chem. Phys. **145**, 074102 (2016).

[25] N. Ricke, M. Welborn, H.-Z. Ye, and T. Van Voorhis, "Performance of Bootstrap Embedding for long-range iinteraction and 2D systems," Mol. Phys. , 1–12 (2017).

[26] T. Tsuchimochi, M. Welborn, and T. Van Voorhis, "Density matrix embedding in an antisymmetrized genimal power bath," J. Chem. Phys. **143**, 024107 (2015).

[27] B. Sandhoefer and G. K.-L. Chan, "Density matrix embedding theory for interacting electron-phonon systems," Phys. Rev. B **94**, 085115 (2016).

[28] B.-X. Zheng and G. K.-L. Chan, "Ground-state phase diagram of the square lattice Hubbard model from density matrix embedding theory," Phys. Rev. B: Condens. Matter Mater. Phys. **93**, 035126 (2016).

[29] J. LeBlanc, A. Antipov, F. Becca, I. Bulik, G. Chan, C.-M. Chung, Y. Deng, M. Ferrero, T. Henderson, C. Jiménez-Hoyos, E. Kozik, X.-W. Liu, A. Millis, N. Prokofiev, M. Qin, G. Scuseria, H. Shi, B. Svistunov, L. Tocchio, I. Tupitsyn, S. R. White, S. Zhang, B.-X. Zheng, Z. Zhu, and E. Gull, "Solutions of the Two-Dimensional Hubbard Model: Benchmarks and Results from a Wide Range of Numerical Algorithms," Phys. Rev. X **5**, 041041 (2015).

[30] Q. Chen, G. H. Booth, S. Sharma, G. Knizia, and G. K.-L. Chan, "Intermediate and spin-liquid phase of the half-filled honeycomb Hubbard model," Phys. Rev. B: Condens. Matter Mater. Phys. **89**, 165134 (2014).

[31] Z. Fan and Q. lin Jie, "Cluster density matrix embedding theory for quantum spin systems," Phys. Rev. B: Condens. Matter Mater. Phys. **91**, 195118 (2015).

[32] S. Wouters, C. A. Jimenez-Hoyos, Q. Sun, and G. K.-L. Chan, "A Practical Guide to Density Matrix Embedding Theory in Quantum Chemistry," J. Chem. Theory Comput. **12**, 2706–2719 (2016).

[33] H. Q. Pham, V. Bernales, and L. Gagliardi, "Can density matrix embedding theory with the complete activate space self-consistent field solver describe single and double bond breaking in molecular systems?" Journal of Chemical Theory and Computation **14**, 1960–1968 (2018), pMID: 29481744, https://doi.org/10.1021/acs.jctc.7b01248.

[34] M. R. Hermes and L. Gagliardi, "Multiconfigurational self-consistent field theory with density matrix embedding: The localized active space self-consistent field method," Journal of Chemical Theory and Computation **15**, 972–986 (2019), pMID: 30620876, https://doi.org/10.1021/acs.jctc.8b01009.

[35] J. S. Kretchmer and G. K.-L. Chan, "A real-time extension of density matrix embedding theory for non-equilibrium electron dynamics," The Journal of Chemical Physics **148**, 054108 (2018), https://doi.org/10.1063/1.5012766.

[36] Z.-H. Cui, T. Zhu, and G. K.-L. Chan, "Efficient implementation of ab initio quantum embedding in periodic systems: Density matrix embedding theory," Journal of Chemical Theory and Computation **16**, 119–129 (2020), pMID: 31815466, https://doi.org/10.1021/acs.jctc.9b00933.

[37] H. Q. Pham, M. R. Hermes, and L. Gagliardi, "Periodic electronic structure calculations with the density matrix embedding theory," Journal of Chemical Theory and Computation **16**, 130–140 (2020), pMID: 31815455, https://doi.org/10.1021/acs.jctc.9b00939.

[38]K. Gunst, S. Wouters, S. D. Baerdemarcker, and D. Van Neck, "Block product density matrix embedding theory for strongly correlated spin systems," Phys. Rev. B **95**, 195127 (2017).

[39]G. H. Booth and G. K.-L. Chan, "Spectra functions of strongly correlated extended systems via an exact quantum embedding," Phys. Rev. B **91**, 155107 (2015).

[40]H. K. Tran, T. Van Voorhis, and A. J. W. Thom, "Using scf metadynamics to extend density matrix embedding theory to excited states," The Journal of Chemical Physics **151**, 034112 (2019), https://doi.org/10.1063/1.5096177.

[41]H.-Z. Ye, M. Welborn, N. D. Ricke, and T. Van Voorhis, "Incremental embedding: A density matrix embedding scheme for molecules," The Journal of Chemical Physics **149**, 194108 (2018), https://doi.org/10.1063/1.5053992.

[42]H.-Z. Ye, N. D. Ricke, H. K. Tran, and T. Van Voorhis, "Bootstrap embedding for molecules," Journal of Chemical Theory and Computation **15**, 4497–4506 (2019), pMID: 31343878, https://doi.org/10.1021/acs.jctc.9b00529.

[43]H.-Z. Ye and T. Van Voorhis, "Atom-based bootstrap embedding for molecules," The Journal of Physical Chemistry Letters **10**, 6368–6374 (2019), pMID: 31578867, https://doi.org/10.1021/acs.jpclett.9b02479.

[44]H.-Z. Ye, H. K. Tran, and T. Van Voorhis, "Bootstrap embedding for large molecular systems," Journal of Chemical Theory and Computation **16**, 5035–5046 (2020), pMID: 32589842, https://doi.org/10.1021/acs.jctc.0c00438.

[45]K. D. Vogiatzis, M. V. Polynski, J. K. Kirkland, J. Townsend, A. Hashemi, C. Liu, and E. A. Pidko, "Computational approach to molecular catalysis by 3d transition metals: Challenges and opportunities," Chemical Reviews **119**, 2453–2523 (2019), https://doi.org/10.1021/acs.chemrev.8b00361.

[46]P. Huo, C. Uyeda, J. D. Goodpaster, J. C. Peters, and T. F. Miller, "Breaking the correlation between energy costs and kinetic barriers in hydrogen evolution via a cobalt pyridinediimine-dioxime catalyst," ACS Catalysis **6**, 6114–6123 (2016), https://doi.org/10.1021/acscatal.6b01387.

[47]M. Moral, L. Muccioli, W.-J. Son, Y. Olivier, and J. C. Sancho-García, "Theoretical rationalization of the singlet–triplet gap in oleds materials: Impact of charge-transfer character," Journal of Chemical Theory and Computation **11**, 168–177 (2015), pMID: 26574215, https://doi.org/10.1021/ct500957s.

[48]S. Ghosh, C. J. Cramer, D. G. Truhlar, and L. Gagliardi, "Generalized-active-space pair-density functional theory: an efficient method to study large, strongly correlated, conjugated systems," Chem. Sci. **8**, 2741–2750 (2017).

[49]M. W. Schmidt and M. S. Gordon, "The construction and interpretation of MCSCF wavefunctions," Annu. Rev. Phys. Chem. **49**, 233–266 (1998).

[50]C. A. Jiménez-Hoyos, R. Rodríguez-Guzmán, and G. E. Scuseria, "Polyradical character and spin frustration in fullerene molecules: An ab initio non-collinear hartree–fock study," The Journal of Physical Chemistry A **118**, 9925–9940 (2014), pMID: 25254432, https://doi.org/10.1021/jp508383z.

[51]J. Lee and M. Head-Gordon, "Distinguishing artificial and essential symmetry breaking in a single determinant: approach and application to the c60, c36, and c20 fullerenes," Phys. Chem. Chem. Phys. **21**, 4763–4778 (2019).

[52]G. Guennebaud, B. Jacob, *et al.*, "Eigen v3," http://eigen.tuxfamily.org (2010).

[53]Q. Sun, T. C. Berkelbach, N. S. Blunt, G. H. Booth, S. Guo, Z. Li, J. Liu, J. D. McClain, E. R. Sayfutyarova, S. Sharma, S. Wouters, and G. K.-L. Chan, "Pyscf: the python-based simulations of chemistry framework," WIREs Comput Mol Sci **8**, e1340 (2017), https://onlinelibrary.wiley.com/doi/pdf/10.1002/wcms.1340.

[54]E. C. Barnes, G. A. Petersson, J. A. Montgomery, M. J. Frisch, and J. M. L. Martin, "Unrestricted coupled cluster and brueckner doubles variations of w1 theory," Journal of Chemical Theory and Computation **5**, 2687–2693 (2009), pMID: 26631782, https://doi.org/10.1021/ct900260g.

[55]W. J. Hehre, R. F. Stewart, and J. A. Pople, "Self-Consistent Molecular-Orbital Methods. I. Use of Gaussian Expansions of Slater-Type Atomic Orbitals," J. Chem. Phys. **51**, 2657 (1969).

[56]P. O. Lowdin, "Quantum Theory of Many-Particle Systems. I. Physical Interpretations," Phys. Rev. **97**, 1474 (1955).

[57]B. O. Roos, P. R. Taylor, and P. E. Sigbahn, "A complete active space scf method (casscf) using a density matrix formulated super-ci approach," Chemical Physics **48**, 157 – 173 (1980).

[58]P. Siegbahn, A. Heiberg, B. Roos, and B. Levy, "A comparison of the super-CI and the newton-raphson scheme in the complete active space SCF method," Physica Scripta **21**, 323–327 (1980).

[59]P. E. M. Siegbahn, J. Almlöf, A. Heiberg, and B. O. Roos, "The complete active space scf (casscf) method in a newton–raphson formulation with application to the hno molecule," The Journal of Chemical Physics **74**, 2384–2396 (1981), https://doi.org/10.1063/1.441359.

[60]R. S. Mulliken, "Electronic population analysis on lcao–mo molecular wave functions. i," The Journal of Chemical Physics **23**, 1833–1840 (1955), https://doi.org/10.1063/1.1740588.

[61]C. Møller and M. S. Plesset, "Note on an approximation treatment for many-electron systems," Phys. Rev. **46**, 618–622 (1934).

[62]O. Gunnarsson and B. I. Lundqvist, "Exchange and correlation in atoms, molecules, and solids by the spin-density-functional formalism," Phys. Rev. B. **13**, 4274 (1977).

[63]J. Gavnholt, T. Olsen, M. Engelund, and J. Schiotz, "Delta Self-Consistent Field as a method to obtain potential energy surfaces of excited molecules on surfaces," Phys. Rev. B **78**, 075441 (2008).

[64]H.-Z. Ye, M. Welborn, N. D. Ricke, and T. Van Voorhis, "σ-scf: A direct energy-targeting method to mean-field excited states," The Journal of Chemical Physics **147**, 214104 (2017), https://doi.org/10.1063/1.5001262.

[65]H.-Z. Ye and T. Van Voorhis, "Half-projected σ-self-consistent field for electronic excited states," Journal of Chemical Theory and Computation **15**, 2954–2965 (2019), pMID: 30995060, https://doi.org/10.1021/acs.jctc.8b01224.